INTERNATIONAL JOURNAL FOR NUMERICAL METHODS IN FLUIDS, VOL. 25, 1057–1082 (1997)

AN EFFICIENT FINITE DIFFERENCE TECHNIQUE FOR COMPUTING INCOMPRESSIBLE VISCOUS FLOWS

M. LOUAKED,* L. HANICH AND K. D. NGUYEN

Département de Mathématiques et Mécanique, Université de Caen, F-14032 Caen Cedex, France

SUMMARY

An improved Navier–Stokes solver is presented to compute two-dimensional incompressible flows in the stream–vorticity formulation at high Reynolds number. The technique is based on both the IMM for the non-orthogonal co-ordinate system and a specialized TVD scheme to cope with non-linear transport terms. Numerical results are shown to demonstrate the accuracy and efficiency of the technique. The method is robust and holds promise to handle complex geometries economically. © 1997 John Wiley & Sons, Ltd.

Int. J. Numer. Meth. Fluids, **25**: 1057–1082 (1997)

No. of Figures: 37. No. of Tables: 2. No. of References: 27.

KEY WORDS: IMM; TVD; flux limiters; non-orthogonal grid

1. INTRODUCTION

The interpolation matrix method (IMM) is a finite difference technique to discretize the multidimensional Navier–Stokes equations in a generalized co-ordinate system. The advantage of the IMM, as pointed out by Koshizuka *et al.*,[1] in comparison with the finite element method is the simplicity in formulating and coding, since the number of points involved is always kept constant (five points for a 2D flow problem) in every pressure-linked equation. This allows the use of classical techniques such as SOR to solve the algebraic equation system.

In Koshizuka's IMM (initial version) the crossing terms are not taken into account. This is only correct when the co-ordinate system is orthogonal, but is false in the contrary case.

Nguyen and En-Nefkhaoui[2] have shown that the absence of crossing terms can produce significant relative error on the vorticity in an inclined cavity flow. They proposed an improved approximate second-order parabolic function. Unfortunately, this remedy is not enough when one simulates complicated fluid flow problems at high Reynolds numbers. An efficient numerical scheme for handling the convective terms is needed. A major difficulty appears when one attempts to improve the method within the special structure of the IMM. In fact, a meticulous observation shows that only methods having certain similarities to Taylor's development are worthwhile candidates.[3–6]

This problem can be resolved by using a higher-order method such as the total-variation-diminishing (TVD) scheme.[7,21,22,25–27] This is achieved by first adapting the Lax–Wendroff (LW)

---

[*] Correspondence to: M. Louaked, Département de Mathématiques et Mécanique, Université de Caen, F-14032 Caen Cedex, France.

CCC 0271–2091/97/091057–26 $17.50

Received January 1997

scheme to the IMM and then updating it to be like the TVD form by appending suitable curvilinear terms. This approach is similar to that used by Davis,[8] inspired by Sweby's interpretation of the LW scheme.[9] This provides a robust treatment for convective terms at high Reynolds numbers by damping the spurious wiggles and remains stable for discontinuous flow parameters even in the zero-viscosity limit.

The aim of this paper is to present a numerical technique that is based on the IMM coupled with a TVD scheme to calculate Navier–Stokes flows at high Reynolds number in arbitrary geometries. Section 2 and 3 describe the numerical background of the IMM. The adaptation of Davis' TVD scheme to the IMM is presented in Section 4. We present several benchmarks to validate the proposed technique and discuss the obtained results in Section 5.

2. GOVERNING EQUATIONS

The stream–vorticity formulation of the Navier–Stokes equations consists of the vorticity transport equation and the Poisson equation for the stream field. Thus for a two-dimensional unsteady incompressible viscous flow the dimensionless governing equations can be expressed in a two-dimensional Cartesian co-ordinate system as

$$\frac{\partial \omega}{\partial t} + u\frac{\partial \omega}{\partial x} + v\frac{\partial \omega}{\partial y} = \frac{1}{Re}\Delta\omega, \tag{1}$$

$$\omega = \frac{\partial v}{\partial y} - \frac{\partial u}{\partial y} \equiv -\Delta\psi, \tag{2}$$

$$u = \frac{\partial \psi}{\partial y}, \qquad v = -\frac{\partial \psi}{\partial x}, \tag{3}$$

where ψ is the streamfunction, ω is the vorticity, (u, v) is the vector velocity and Re is the Reynolds number.

3. IMM METHOD

3.1. General framework

In the IMM discretization one assumes a polynomial expression of any physical quantity ϕ by some nodal values in the neighbourhood of a mesh point P:

$$\phi(x) = \sum_{k=0}^{n} C_k^p P_k(x). \tag{4}$$

The differential coefficients of the physical quantity at mesh point P are obtained by differentiating equation (4):

$$\frac{\partial \phi}{\partial x_j} = \sum_{k=0}^{n} C_k^p \frac{\partial P_k}{\partial x_j}. \tag{5}$$

Equation (5) can be written in matrix form as

$$D(P) = M_D(P)\Phi(P), \tag{6}$$

where $D(P)$ is a vector of the $n+1$ differential coefficients. Here the vector $\Phi(P)$ consists of the $n+1$ nodal values of the physical quantity, while the matrix $M_D(P)$ depends only on $\Phi(P)$ and the functions of the polynomial as shown on the right-hand side of equations (4) and (5).

The IMM provides a way of making a convenient transformation between a local, computational space (natural co-ordinates) and global, physical space. Figure 1 shows the geometry in both physical and natural co-ordinate space.

Now we define the approximate polynomial equation (4) in the transformed plane. The interpolating matrix $M_D(P)$ in terms of the ξ-co-ordinate system reads

$$D_\xi(P) = M_{D_\xi}\Phi(P). \tag{7}$$

The interpolating matrix M_{D_ξ} is assumed to be homogeneous for every mesh point P. With the help of the transformation matrix $T_{\xi\to x}$ defined as

$$D(P) = T_{\xi\to x}D_\xi(P), \tag{8}$$

the following expression for the interpolating matrix $M_D(P)$ in terms of the x-co-ordinate system is obtained:

$$M_D(P) = T_{\xi\to x}M_{D_\xi}. \tag{9}$$

Here the matrix $T_{\xi\to x}$ involves terms such $x_\xi, x_\eta, x_{\xi\xi}, \ldots$. Note that the basis functions used in the trial function expansion are also used to define the co-ordinate mapping; the co-ordinate mapping is referred to as an 'isoparametric co-ordinate transformation'.

3.2. *Typical interpolation*

Biquadratic shape functions are used. Thus for a quantity ϕ one can write

$$\phi = c_0 + c_1\xi + c_2\eta + c_3\xi^2 + c_4\eta^2 + c_5\xi\eta + c_6\xi^2\eta + c_7\xi\eta^2 + c_8\xi^2\eta^2. \tag{10}$$

Note that at point P the higher-order mixed derivatives of ϕ are equal to zero, except for the lowest-order one $\phi_{\xi\eta=c_5}$. The ξ- and η-derivatives of ϕ are given as

$$\begin{pmatrix} \phi_\xi \\ \phi_\eta \\ \phi_{\xi\xi} \\ \phi_{\eta\eta} \\ \phi_{\xi\eta} \end{pmatrix} = \begin{pmatrix} 0 & -\frac{1}{2} & \frac{1}{2} & 0 & 0 \\ -\frac{1}{2} & 0 & 0 & \frac{1}{2} & 0 \\ 0 & 1 & 1 & 0 & 0 \\ 1 & 0 & 0 & 1 & 0 \\ 0 & 0 & 0 & 0 & \frac{1}{4} \end{pmatrix} \begin{pmatrix} \phi_1 - \phi_0 \\ \phi_2 - \phi_0 \\ \phi_3 - \phi_0 \\ \phi_4 - \phi_0 \\ \phi_5 + \phi_8 - \phi_6 - \phi_7 \end{pmatrix}. \tag{11}$$

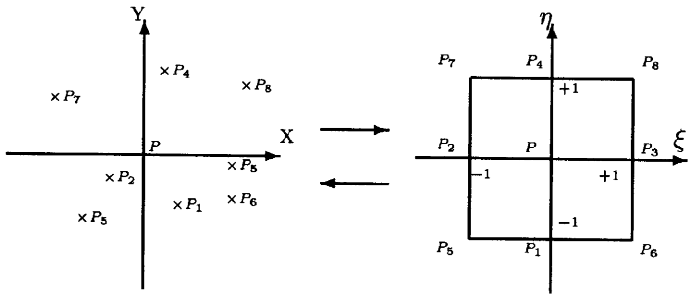

Figure 1. Co-ordinate transformations between physical space and natural space

Here ϕ_i $(i = 1, \ldots, 8)$ represents the ϕ-variable values at point P_i. The derivatives in the (x, y)- and (ξ, η)-coordinate systems are related as

$$\begin{pmatrix} \phi_x \\ \phi_y \\ \phi_{xx} \\ \phi_{yy} \\ \phi_{xy} \end{pmatrix} = \begin{pmatrix} \xi_\xi & \eta_x & 0 & 0 & 0 \\ \xi_y & \eta_y & 0 & 0 & 0 \\ \xi_{xx} & \eta_{xx} & \xi_x^2 & \eta_x^2 & 2\xi_x\eta_x \\ \xi_{yy} & \eta_{yy} & \xi_y^2 & \eta_y^2 & 2\xi_y\eta_y \\ \xi_{xy} & \eta_{xy} & \xi_x\xi_y & \eta_x\eta_y & \xi_x\eta_y + \xi_y\eta_x \end{pmatrix} \begin{pmatrix} \phi_\xi \\ \phi_\eta \\ \phi_{\xi\xi} \\ \phi_{\eta\eta} \\ \phi_{\xi\eta} \end{pmatrix}. \tag{12}$$

The combination of equations (11) and (12) gives

$$\begin{pmatrix} \phi_x \\ \phi_y \\ \phi_{xx} \\ \phi_{yy} \\ \phi_{xy} \end{pmatrix} = \underbrace{[IM] \begin{pmatrix} \phi_1 - \phi_0 \\ \phi_2 - \phi_0 \\ \phi_3 - \phi_0 \\ \phi_4 - \phi_0 \end{pmatrix}}_{\text{I}} + \underbrace{\begin{pmatrix} 0 \\ 0 \\ 2\xi_x\eta_x\phi_{\text{m}} \\ 2\xi_y\eta_y\phi_{\text{m}} \\ (\xi_x\eta_y + \xi_y\eta_x)\phi_{\text{m}} \end{pmatrix}}_{\text{II}}, \tag{13}$$

where

$$[IM] = \begin{pmatrix} -\eta_x/2 & -\xi_x/2 & \xi_x/2 & \eta_x/2 \\ -\eta_y/2 & -\xi_y/2 & \xi_y/2 & \eta_y/2 \\ -\eta_{xx}/2 + \eta_x^2 & -\xi_{xx}/2 + \xi_x^2 & \xi_{xx}/2 + \xi_x^2 & \eta_{yy}/2 + \eta_x^2 \\ -\eta_{yy}/2 + \eta_y^2 & -\xi_{yy}/2 + \xi_y^2 & \xi_{yy}/2 + \xi_y^2 & \eta_{22}/2 + \eta_y^2 \\ -\eta_{xy}/2 + \eta_x\eta_y & -\xi_{xy}/2 + \xi_x\xi_y & \xi_{xy}/2 + \xi_x\xi_y & \eta_{xy}/2 + \eta_x\eta_y \end{pmatrix} \tag{14}$$

is called the interpolating matrix and $\phi_{\text{m}} = (\phi_5 - \phi_6 + \phi_8 - \phi_7)/4$. Terms I in equation (13) represents a central approximation of the first- and second-order derivatives and term II is a correction to the second-order derivatives when the co-ordinate transformation is non-orthogonal.

4. NUMERICAL SCHEME

4.1. Review of Sweby's scheme and Davis' approach

In order to introduce Sweby's scheme[9] in a simple setting, we consider the scalar wave equation

$$\frac{\partial\omega}{\partial t} + a\frac{\partial\omega}{\partial x} = 0. \tag{15}$$

Let ω_j^n be the numerical solution of (15) at $x = j\Delta x$, $t = n\Delta t$, with Δx the mesh spacing and Δt the time step. If we assume $a > 0$, then the Lax–Wendroff method is written as the upwind part with an additional antidiffusive flux:

$$\omega_j^{n+1} = \omega_j^n - v\Delta\omega_{j-1/2}^n - \nabla[\tfrac{1}{2}(1 - v)v\Delta\omega_{j+1/2}^n], \tag{16}$$

where $v = a\Delta t/\Delta x$, $\Delta\omega_{j-1/2}^n = \omega_j^n - \omega_{j-1}^n$ and $\Delta\omega_{j+1/2}^n = \omega_{j+1}^n - \omega_j^n$.

Since the first-order scheme does not produce spurious oscillations at discontinuities, a limited amount of antidiffusive flux is added:

$$-\nabla[\phi\,\tfrac{1}{2}(1-v)v\Delta\omega^n_{j+1/2}]. \tag{17}$$

A particular form of the resulting scheme is given by the incremental form

$$\omega_j^{n+1}=\omega_j^n-v\{1+\tfrac{1}{2}(1-v)[\phi(r_j^+)/r_j^+-\phi(r_{j-1}^+)]\}\Delta\omega^n_{j=1/2} \tag{18}$$

where $r_j^+=\Delta\omega^n_{j-1/2}/\Delta\omega^n_{j+1/2}$.

Algebraic conditions on the limiter function which guarantee the TVD property are

$$0\leqslant[\phi(r)/r,\,\phi(r)]\leqslant 2, \tag{19}$$

provided that the CFL condition $v\leqslant 1$ is realized. Davis[8] showed that it is possible to recover Sweby's scheme by adding suitable terms to the Lax–Wendroff method:

$$[K^+(r_j^+)]\Delta\omega^n_{j+1/2}-[K^+(r_{j-1}^+)]\Delta\omega^n_{j-1/2}. \tag{20}$$

The resulting scheme can be written as

$$\omega_j^{n+1}=\omega_j^n-\frac{v}{2}(\omega^n_{j+1}-\omega^n_{j-1})+\frac{v^2}{2}(\omega^n_{j+1}-2\omega^n_j+\omega^n_{j-1})+[K^+(r_j^+)]\Delta\omega^n_{j+1/2}-[K^+(r_{j-1}^+)]\Delta\omega^n_{j-1/2}. \tag{21}$$

Sweby's scheme is obtained by choosing

$$K^+(r_j^+)=\frac{v}{2}(1-v)[1-\phi(r_j^+)]. \tag{22}$$

4.2. *Formulation of proposed extension to IMM*

In the IMM the differential coefficients in Cartesian space are estimated at each mesh point and the differential equation is directly transformed to a difference equation. The one-step LW scheme for the two-dimensional vorticity convection equation is obtained from equation (1),

$$\frac{\partial\omega}{\partial t}+\frac{\partial u\omega}{\partial x}+\frac{\partial v\omega}{\partial x}=0, \tag{23}$$

and written in IMM difference operator notation as

$$\bar{\omega}^n_{ij}=\omega^n_{ij}-\Delta t\delta_x(u\omega)^n-\Delta t\delta_y(v\omega)^n+\frac{\Delta t^2}{2}u[\delta_{xx}(u\omega)^n+\delta_{xy}(v\omega)^n]+\frac{\Delta t^2}{2}v[\delta_{yy}(v\omega)^n+\delta_{yx}(u\omega)^n], \tag{24}$$

where the IMM difference operators are defined by

$$\begin{aligned}\delta_x\phi&=\mathit{coeff}(1,1,ij)(\phi(\mathit{neigh}(1,ij))-\phi(ij))+\mathit{coeff}(2,1,ij)(\mathit{neigh}(2,ij))-\phi(ij))\\&\quad+\mathit{coeff}(3,1,ij)(\phi(\mathit{neigh}(3,ij))-\phi(ij))+\mathit{coeff}(4,1,ij)(\phi(\mathit{neigh}(4,ij))-\phi(ij)), &(25)\\ \delta_{xx}\phi&=\mathit{coeff}(1,3,ij)(\phi(\mathit{neigh}(1,ij))-\phi(ij))+\mathit{coeff}(2,3,ij)(\phi(\mathit{neigh}(2,ij))-\phi(ij))\\&\quad+\mathit{coeff}(3,3,ij)\phi(\mathit{neigh}(3,ij))-\phi(ij))+\mathit{coeff}(4,3,ij)(\phi(\mathit{neigh}(4,ij))-\phi(ij), &(26)\\ \delta_{xy}\phi&=\mathit{coeff}(1,5,ij)(\phi(\mathit{neigh}(1,ij))-\phi(ij))+\mathit{coeff}(2,5,ij)(\phi(\mathit{neigh}(2,ij))-\phi(ij))\\&\quad+\mathit{coeff}(3,5,ij)(\phi(\mathit{neigh}(3,ij))-\phi(ij))+\mathit{coeff}(4,5,ij)(\phi(\mathit{neigh}(4,ij))-\phi(ij). &(27)\end{aligned}$$

Here *coeff*(., ., *ij*) represents the differential coefficient in the interpolating matrix at mesh point *ij*. Similar equations for δ_y and δ_{yy} can be determined from (25) and (26) by replacing the second column of *coeff*(., ., *ij*) the numbers 1 and 3 by 2 and 4 respectively. The term *neigh*(n, *ij*) is the reference of the point P_n neighbour of mesh point *ij*.

As the proposed scheme produces spurious wiggles in solutions with steep gradients, the scheme (24) can be updated to TVD form by appending to the right-hand side of equation (24) suitable curvilinear terms (see Appendix A)

$$\begin{aligned}&[K^+(rx^+_{i,j}) + K^-(rx^-_{i+1,j})]\Delta\omega^n_{i+1/2,j} - [K^+(rx^+_{i-1,j}) + K^-(rx^-_{i,j})]\Delta\omega^n_{i-1/2,j}\\&\quad + [K^+(ry^+_{i,j}) + K^-(ry^-_{i,j+1})]\Delta\omega^n_{i,j+1/2} - [K^+(ry^+_{i,j-1}K^-(ry^-_{i,j})]\Delta\omega^n_{i,j-1/2},\end{aligned} \tag{28}$$

where

$$K^+(rx^+_{i,j}) = \begin{cases}(cp1 + cp2)[1 - \phi(rx^+_{i,j})] & \text{if } u_{ij} > 0,\\ 0 & \text{if } u_{ij} < 0,\end{cases} \tag{29}$$

with

$$\begin{aligned}cp1 &= \Delta t u_{ij}(coeff(3, 1, ij) - 0{\cdot}5\Delta t u_{ij} coeff(3, 3, ij)),\\ cp2 &= \Delta t v_{ij}(coeff(3, 2, ij) - 0{\cdot}5\Delta t v_{ij} coeff(3, 4, ij)),\end{aligned} \tag{30}$$

and

$$K^-(rx^-_{i+1,j}) = \begin{cases}(c\bar{p}1 + c\bar{p}2)[1 - \phi(rx^-_{i+1,j})] & \text{if } u_{ij} < 0,\\ 0 & \text{if } u_{ij} > 0,\end{cases} \tag{31}$$

with

$$\begin{aligned}c\bar{p}1 &= -\Delta t u_{ij}(coeff(3, 1, ij) + 0{\cdot}5\Delta t u_{ij} coeff(3, 3, ij)),\\ c\bar{p}2 &= -\Delta t v_{ij}(coeff(3, 2, ij) + 0{\cdot}5\Delta t v_{ij} coeff(3, 4, ij)).\end{aligned} \tag{32}$$

One might measure the smoothness of the data by looking at the ratio of consecutive gradients,

$$rx^+_{i,j} = \frac{\Delta\omega^n_{i=1/2,j}}{\Delta\omega^n_{i+1/2,j}}, \qquad rx^-_{i,j} = \frac{\delta\omega^n_{i+1/2,j}}{\Delta\omega^n_{i-1/2,j}}, \tag{33}$$

where

$$\Delta\omega^n_{i-1/2,j} = \omega^n_{i,j} - \omega^n_{i-1,j}, \qquad \Delta\omega^n_{i,j-1/2} = \omega^n_{i,j} - \omega^n_{i,j-1}. \tag{34}$$

Here $\phi(r)$ is the flux limiter function defined by

$$\phi(r) = \max(0, \min(1, 2r), \min(r, 2)), \tag{35}$$

which is called Roe's 'superbee' limiter.

In the final stage the vorticity values will be corrected by appending the diffusion term. Thus the vorticity value at time step $n+1$ is given by

$$\begin{aligned}\omega^{n+1}_{i,j} &= \bar{\omega}^n_{i,j} + [K^+(rx^+_{i,j}) + K^-(rx^-_{i+1,j})]\Delta\omega^n_{i+1/2,j} - [K^+(rx^+_{i-1,j}) + K^-(rx^-_{i,j})]\Delta\omega^n_{i-1/2,j}\\&\quad + [K^+(ry^+_{i,j}) + K^-(ry^-_{i,j+1}]\Delta\omega^n_{i,j+1/2} - [K^+(ry^+_{i,j-1}) + K^-(ry^-_{i,j})]\Delta\omega^n_{i,j-1/2}\\&\quad + \frac{\Delta t}{Re}(\delta_{xx}\omega^n + \delta_{yy}\omega^n).\end{aligned} \tag{36}$$

where $u^n = \delta_y \psi^n$ and $v^n = -\delta_x \psi^n$. This explicit time discretization is expected to be non-linearly stable under the conditions[10]

$$0{\cdot}5(u^2 + v^2)\Delta t Re \leqslant 1, \qquad \frac{2\Delta t}{Re}\left(\frac{1}{\Delta x^2} + \frac{1}{\Delta y^2}\right) \leqslant 1. \tag{37}$$

5. NUMERICAL TESTS

The benchmark tests presented below are chosen so that the use of non-orthogonal and non-uniform grids will be inevitable to ensure the approximate benchmark solution. As the grid non-orthogonality strongly affects the numerical errors and the convergence of the computed results, the first two tests involve a lid-driven, inclined cavity flow. The computational grid used must be parallel to the sidewalls and then necessarily non-orthogonal. The last test deals with the flow past a circular cylinder. A lot of successive flow patterns behind the cylinder at different Reynolds number values have been observed by numerical and experimental methods.[11–13]

The proposed model must be able to simulate the time evolution of these flow patterns fairly well. In order to achieve this, an appropriate numerical scheme will be needed to prevent spurious oscillation and numerical diffusion due to strongly convective flows. Additionally, the use of non-uniform grids with variable spacing ratio will be indispensable. Therefore this test permits the evaluation of the accuracy and reliability of the model as a whole. In the next two subsections we will describe the benchmark, present the numerical results and give some discussion.

5.1. Driven cavity flow

We consider the steady flow inside an inclined cavity whose upper lid is moving at constant velocity U_L. This classical problem has become a standard benchmark for assessing the performance of algorithms to solve the incompressible Navier–Stokes equations. The benchmark reference solutions[14,15] provide a tool to check the accuracy and robustness when evaluating a new method in handling complex flows on a non-orthogonal grid.

The domain of calculation in a parallelogram with angle $\beta = 45°$ for test 1 and $\beta = 30°$ for test 2. In both cases the lid velocity $U_\mathrm{L} = 1$, the cavity length $L = 1$ and the density $\rho = 1$. The geometry and corresponding boundary conditions are shown in Figure 2. For tests 1 and 2 the Reynolds number $Re = U_\mathrm{L} L/v = 1000$.

These tests were first proposed by Demirdzic *et al.*[14] as the benchmark reference (BR) for non-orthogonal grid but at two different Reynolds number values $Re = 100$ and 1000. The authors have used a finite volume technique coupled with a SIMPLE method to solve the (u, v, p) primitive variable governing equations. The BR solution has been obtained for both tests using several calculational grids (20×20, 40×40, 80×80, 160×160, 320×320 control volumes (CVs)) in a multigrid procedure. Demirdzic has shown that for both Reynolds numbers the difference between the velocity profiles obtained on the two finest grids is hardly visible. It is also very small on the 80×80 and 320×320 CVs. Consequently, the use of fine grids seems not to be necessary.

We have resolved the problem using a (ψ, ω) formulation and a 120×120 grid. The boundary conditions are those of no slip on the fixed walls, i.e. $u = 0$ and $v = 0$; on the sliding wall, $u = 1$ and $v = 0$. Zero values are prescribed for ψ on the boundary; the vorticity ω on the boundary is obtained using the Poisson equation.

Figures 3 and 4 present the u- and v-velocity component profiles along the centrelines CL1 and CL2 respectively obtained from IMM calculations for $\beta = 45°$ at $Re = 1000$, in comparison with Demirdzic's 320×320 CV results. The difference between them is not visible. The streamline

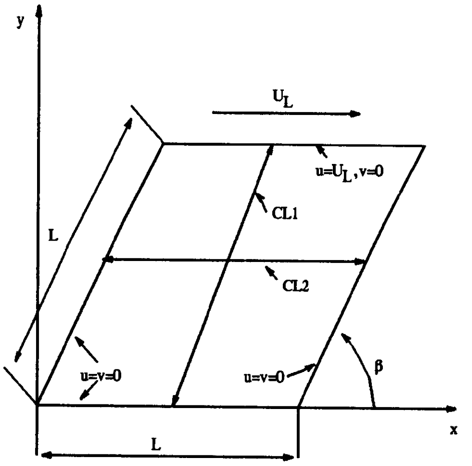

Figure 2. Geometry and boundary conditions for skewed driven cavity problem

contour map for this test is shown in Figure 5. Clearly, we have obtained the same flow pattern as that of Demirdzic. There exist two velocities. According to the growth of *Re*, the primary vortex, driven by the lid motion, becomes smaller and smaller while the secondary vortex size increases; at $Re = 1000$ the primary vortex fills only about the upper third of the cavity, while the secondary vortex becomes larger but weaker. Table I presents the streamfunction values at the centres of the first and second vortices $\psi_{\min}$ and $\psi_{\max}$ respectively, as well as the x- and y-co-ordinates of their positions obtained from Demirdzic and from IMM calculations. Obviously, our results are qualitatively in very good agreement with Demirdzic's results. Figure 6 presents the vorticity contour map. Unfortunately, as Demirdzic did not calculate the vorticity, no comparison is possible.

In the second test for $\beta = 30°$, i.e. for extreme grid non-orthogonality, the results are still similar to those obtained from Demirdzic's calculation. Figures 7 and 8 present the velocity profiles for this test. The difference between the results obtained from the IMM calculation and from Demirdzic is always hardly visible. Because of the smaller volume of the cavity, the primary vortex is two times weaker

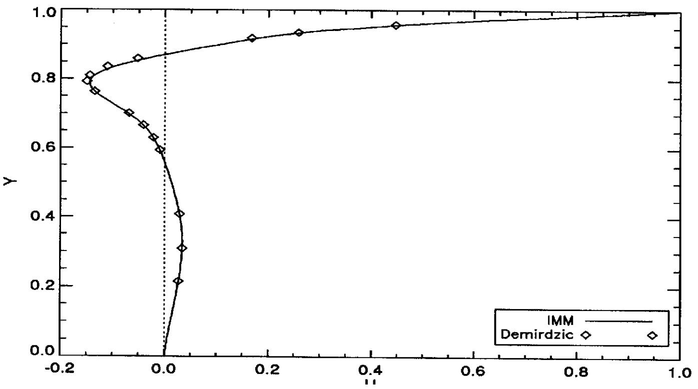

Figure 3. Velocity profiles along CL1 for $\beta = 45°$ and $Re = 1000$

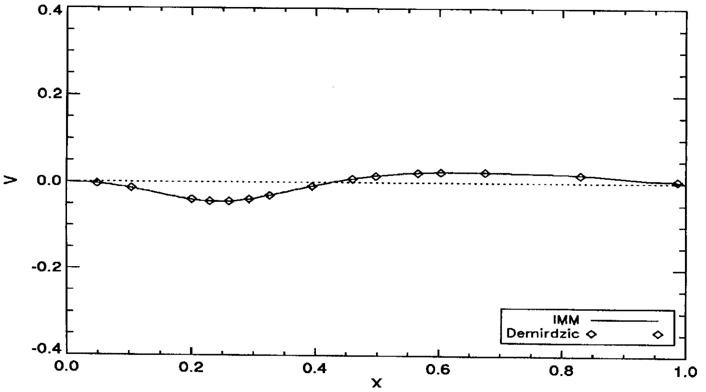

Figure 4. Velocity profiles along CL2 for $\beta = 45°$ and $Re = 1000$

than that of the first test (Figures 9 and 10) by Demirdzic. The IMM results agree fairly well with Demirdzic's. This effectively proves the accuracy and reliability of the proposed model.

In an attempt to give a likely BR solution, we have calculated the flow in the same cavity as in the second test ($\beta = 30°$) but at $Re = 3000$. Figures 11 and 12 present the streamfunction and vorticity contour map for this test. According to this Reynolds number, the primary vortex size is reduced. It fills only about the upper quarter of the cavity. The comparison between the primary vortex in this case with the one obtained in the second test shows that the ratio is about 1·37. Table II presents the minimum and maximum streamfunction values at the vortex centres and their positions for $\beta = 30°$ at $Re = 3000$.

5.2. *Flow around a circular cylinder*

The flow past a circular cylinder is an unsteady problem in nature and good numerical accuracy is required in order to capture the different phenomena present in the non-stationary solution.

In the time development, immediately after the start of the motion the flow is irrotational everywhere. As a function of the Reynolds number, Bouard and Coutanceau[11] pointed out the existence of four kinds of structures in the recirculating zone. At moderate Reynolds numbers the appearance of a bulge in the streamline pattern and the presence of a secondary eddy ($Re \geqslant 550$) with

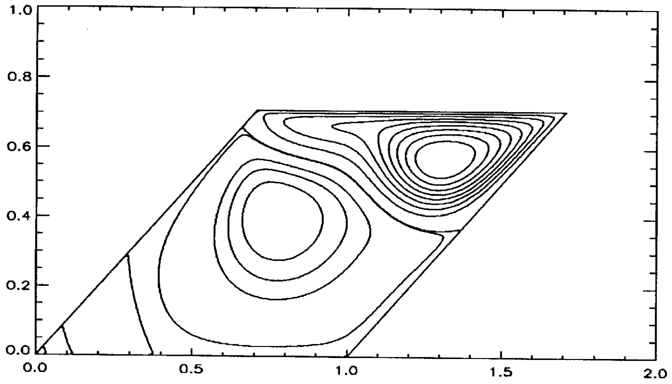

Figure 5. Predicted streamlines for $\beta = 45°$ and $Re = 1000$

Table I. Minimum and maximum streamfunction values at vortex centres and their positions ($Re = 1000$)

	$\beta = 45°$		$\beta = 30°$	
	Demirdzic	IMM	Demirdzic	IMM
$\psi_{\min}$	$-5\cdot3507 \times 10^{-2}$	$-5\cdot469 \times 10^{-2}$	$-3\cdot8563 \times 10^{-2}$	$-3\cdot9000 \times 10^{-2}$
x	1·3130	1·3100	1·4583	1·4540
y	0·5740	0·5700	0·4108	0·4080
$\psi_{\max}$	$1\cdot0039 \times 10^{-2}$	$1\cdot0170 \times 10^{-2}$	$4\cdot1494 \times 10^{-3}$	$4\cdot312 \times 10^{-3}$
x	0·7766	0·7760	0·9038	0·8980
y	0·3985	0·3980	0·2550	0·2560

a rotation opposite to that of the main eddy are found. Then, for Reynolds numbers ranging from 3000 to 9500, a second pair of secondary eddies appears (α and β phenomena).

The aim of this test is to demonstrate the capacity of the IMM to highlight the flow structures at early times of an impulsively started circular cylinder (of diameter $D = 2R$) at Reynolds numbers of 300, 550, 3000 and 9500, for which experimental[11] and numerical[12,13,16–20,23,24] data exist.

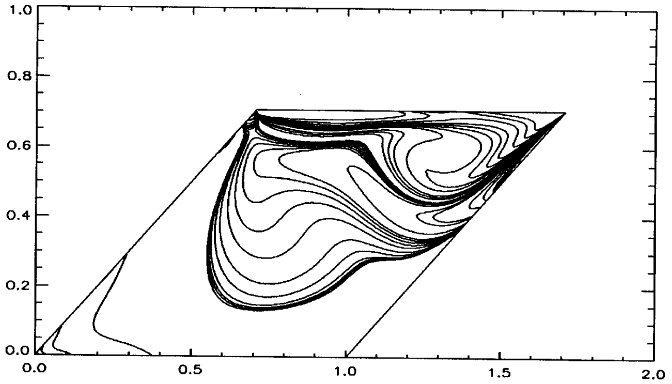

Figure 6. Predicted vorticity lines for $\beta = 45°$ and $Re = 1000$

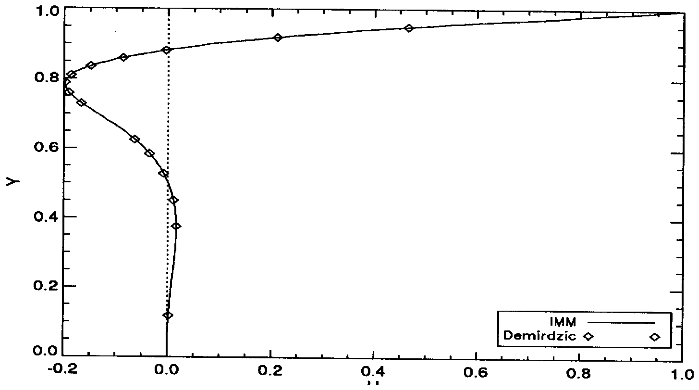

Figure 7. Velocity profiles along CL1 for $\beta = 30°$ and $Re = 1000$

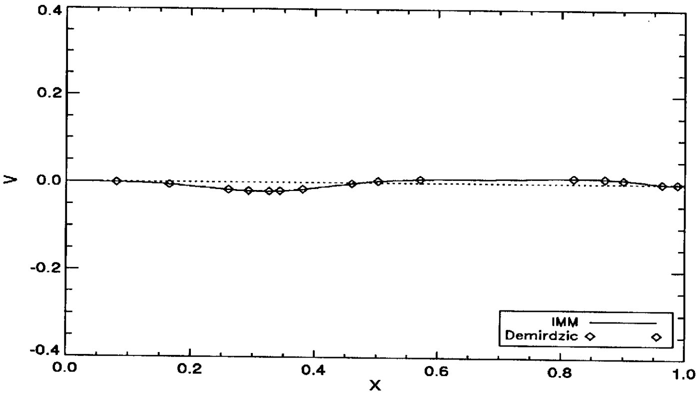

Figure 8. Velocity profiles along CL2 for $\beta = 30^\circ$ and $Re = 1000$

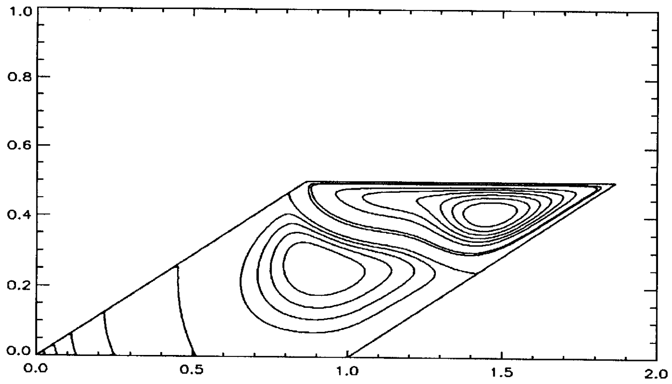

Figure 9. Predicted streamlines for $\beta = 30^\circ$ and $Re = 1000$

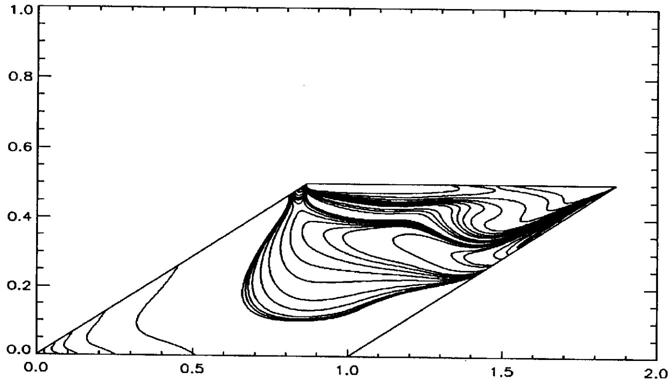

Figure 10. Predicted vorticity lines for $\beta = 30^\circ$ and $Re = 1000$

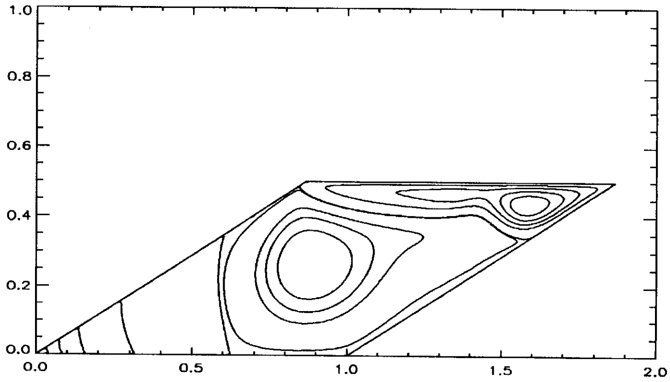

Figure 11. Predicted streamlines for $\beta = 30°$ and $Re = 3000$

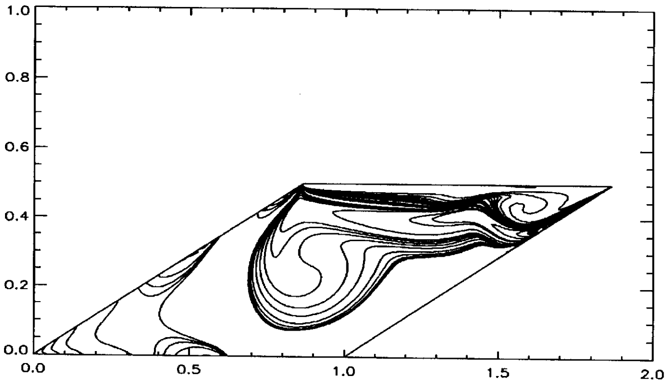

Figure 12. Predicted vorticity lines for $\beta = 30°$ and $Re = 3000$

For time $t \geqslant 0$ a uniform velocity U_∞ is applied to the fluid at infinity. The dimensionless unsteady Navier–Stokes equations, according to time $T = U_\infty t/R$ and Reynolds number $Re = U_\infty D/\nu$, are solved in the domain exterior to the cylinder, with no slip on the cylinder surface and uniform flow conditions at infinity. The domain is discretized into an 81×161 grid with grid points clustered near the cylinder. All the calculations are performed on this grid and any symmetry conditions on the flow are assumed. The time step $\Delta t = 0{\cdot}01$ for $Re = 300$ and 500 and $\Delta t = 0{\cdot}001$ for $Re = 3000$ and 9500. The results are shown in Figures 13–37.

Figures 13, 14, 17, 18, 21, 23, 27 and 28 present the evolution of the streamline patterns for flow at Reynolds numbers between $Re = 300$ and 9500. The evolution from a pair of eddies to the α and β phenomena is clearly seen.

Figures 31–33 show the axial velocity in the region immediately behind the cylinder. A strong recirculating flow can be observed as the primary eddies induce velocities. Compared with the experimental results[11] for $Re = 550$ and the numerical results[12] for $Re = 300$ and 550, the simulation overpredicts the strength of the recirculating flow. However, in Ta Phuoc Loc's results,[12] computed using a fourth-order compact finite difference scheme, an underprediction compared with the experimental solution was observed.

Table II. Minimum and maximum streamfunction values at vortex centres and their positions ($Re = 3000$, $\beta = 30°$)

$\psi_{\min}$	$-2{\cdot}838 \times 10^{-2}$	$\psi_{\max}$	$1{\cdot}0330 \times 10^{-2}$
x	1·5890	x	0·8880
y	0·4370	y	0·2610

For $Re = 3000$, Figures 21–24 compare the Couard and Coutanceau flow visualizations[11] with the computed streamlines for $T = 2$ and 5. The agreement is good. Not only are the size and location of the secondary vortex accurately predicted, but the details of the flow around it are also correctly described.

The time evolution of the geometrical parameter of the wake is shown in Figures 34 and 35 for $Re = 3000$ and 9500 and compared with experimental measurements.[11] The simulation accurately predicts the length of the closed wake.

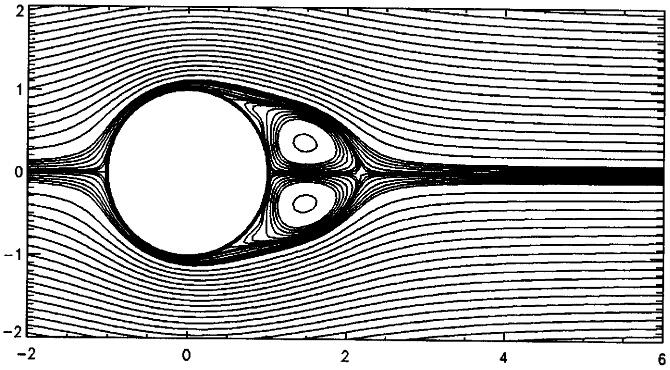

Figure 13. Streamline pattern for $Re = 300$ at $T = 3$

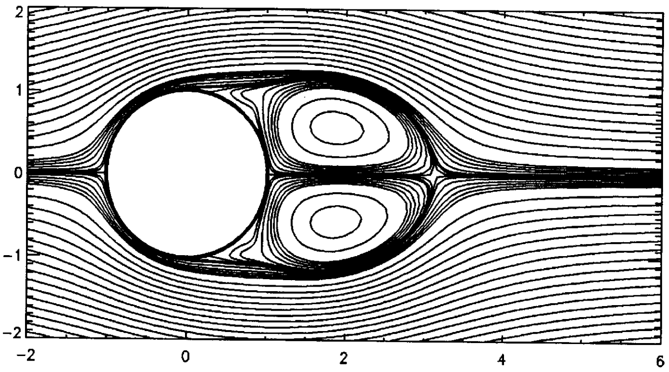

Figure 14. Streamline pattern for $Re = 300$ at $T = 6$

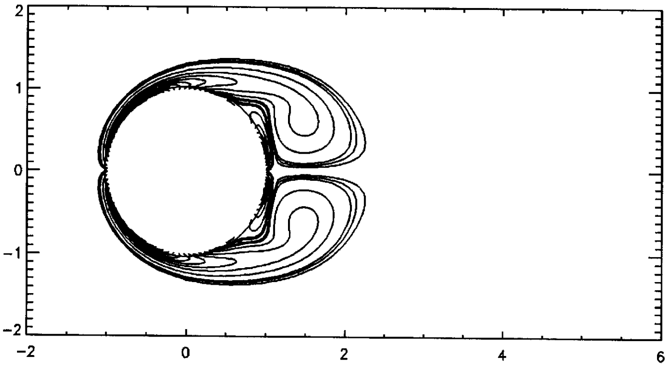

Figure 15. Vorticity lines for $Re = 300$ at $T = 3$

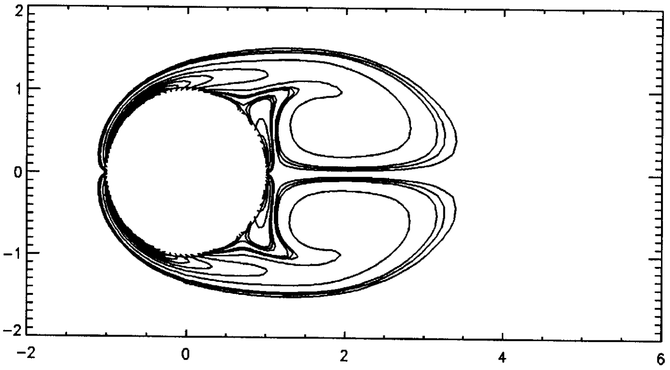

Figure 16. Vorticity lines for $Re = 300$ at $T = 6$

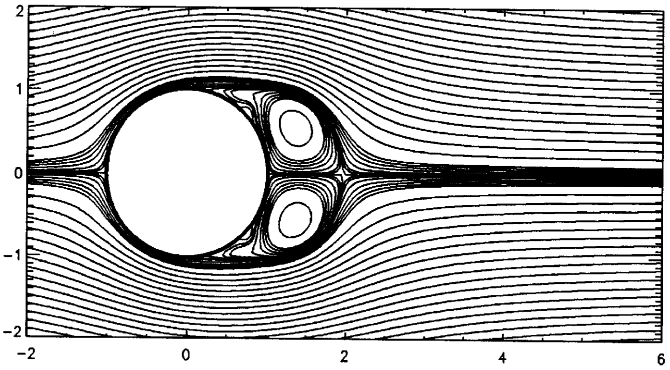

Figure 17. Streamline pattern for $Re = 550$ at $T = 3$

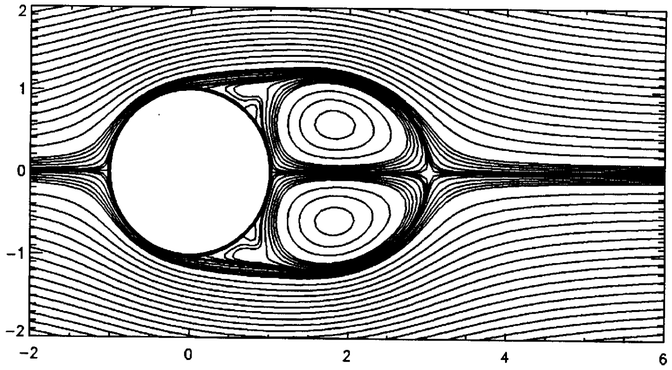

Figure 18. Streamline pattern for $Re = 550$ at $T = 6$

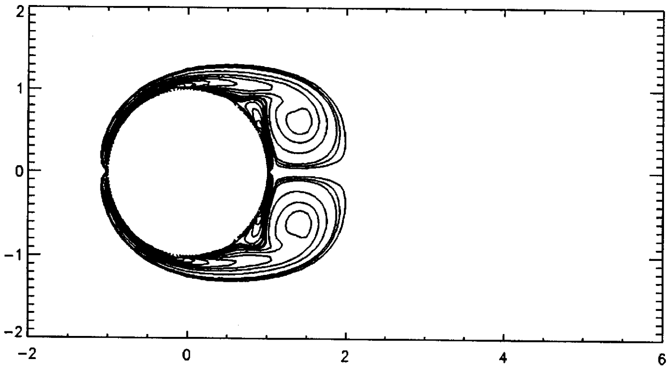

Figure 19. Vorticity lines for $Re = 550$ at $T = 3$

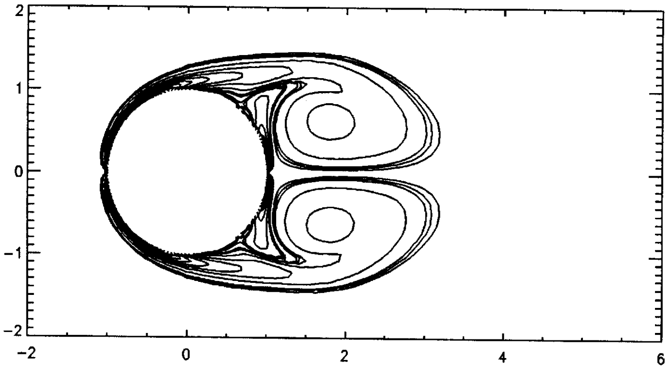

Figure 20. Vorticity lines for $Re = 550$ at $T = 6$

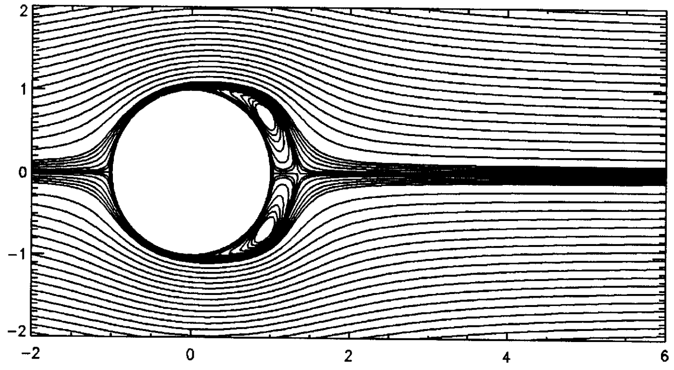

Figure 21. Streamline pattern for $Re = 3000$ at $T = 2$

Figure 22. Experimental visualization of Bouard and Coutanceau[11] for $Re = 3000$ at $T = 2$

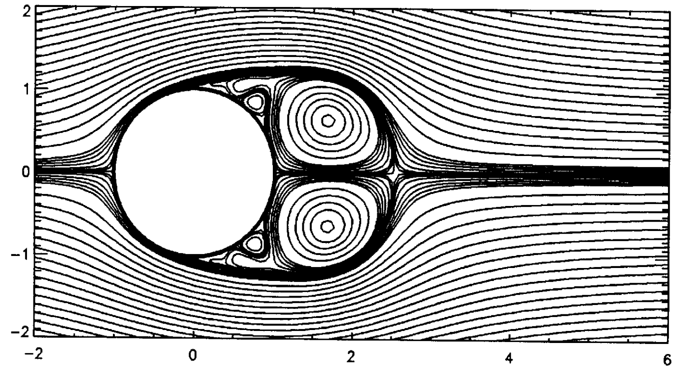

Figure 23. Streamline pattern for $Re = 3000$ at $T = 5$

Figure 24. Experimental visualization of Bouard and Coutanceau[11] for $Re = 3000$ at $T = 5$

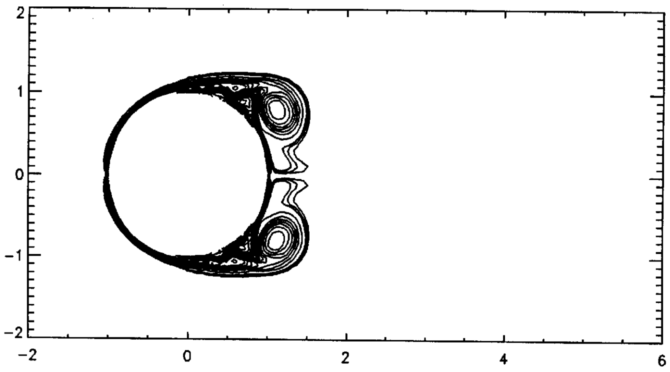

Figure 25. Vorticity lines for $Re = 3000$ at $T = 3$

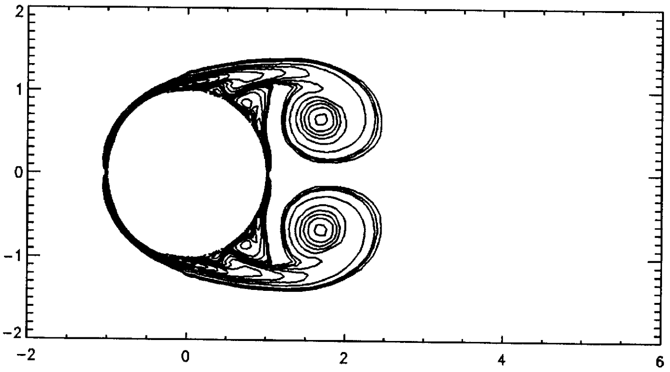

Figure 26. Vorticity lines for $Re = 3000$ at $T = 5$

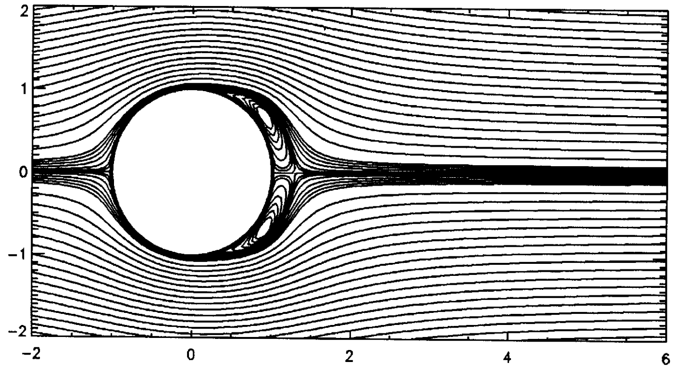

Figure 27. Streamline pattern for $Re = 9500$ at $T = 2$

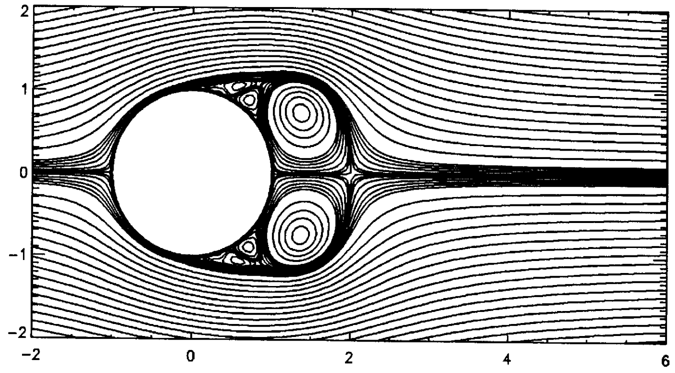

Figure 28. Streamline pattern for $Re = 9500$ at $T = 4$

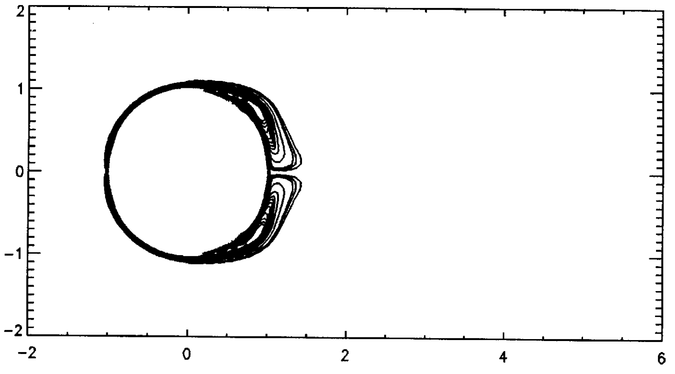

Figure 29. Vorticity lines for $Re = 9500$ at $T = 2$

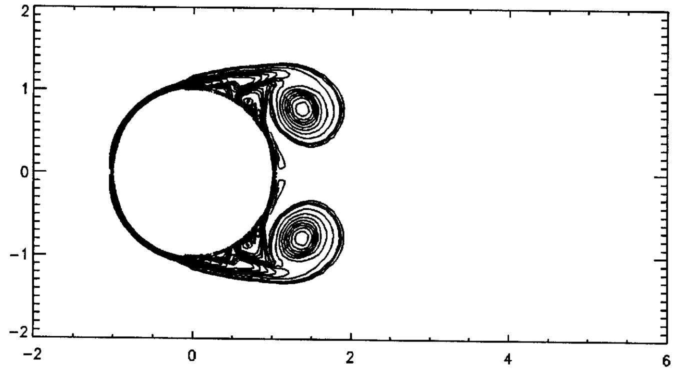

Figure 30. Vorticity lines for $Re = 9500$ at $T = 4$

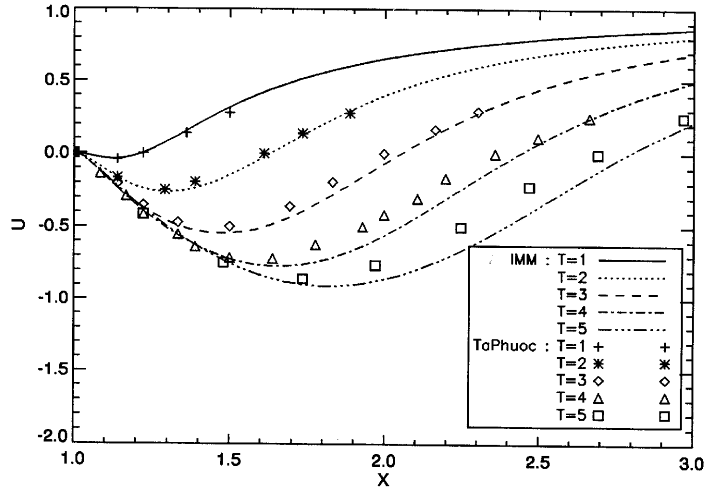

Figure 31. Comparison between IMM and Ta Phuoc Loc[12] numerical results for axial velocity for $Re = 300$

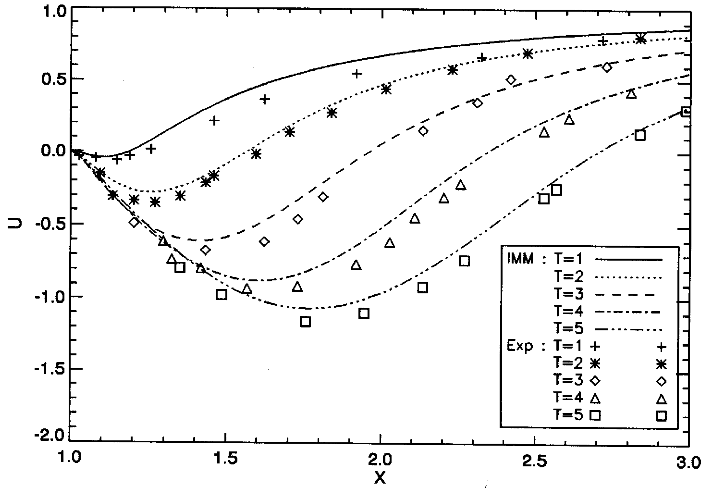

Figure 32. Comparison between experimental and numerical results for axial velocity for $Re = 550$

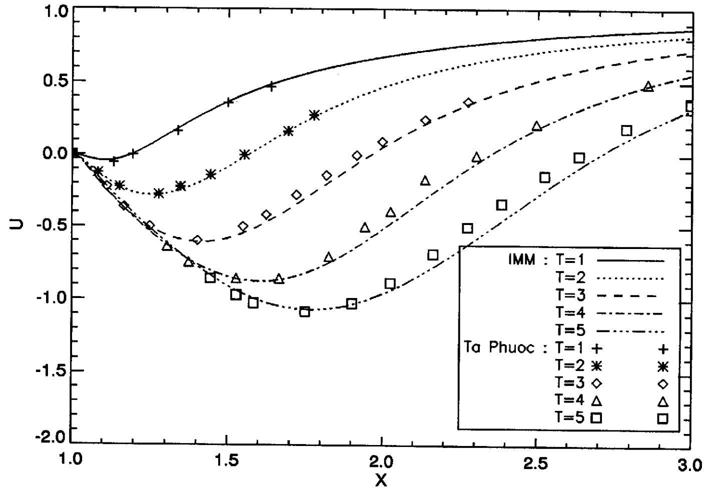

Figure 33. Comparison between IMM and Ta Phuoc Loc[12] numerical results for axial velocity for $Re = 550$

6. CONCLUDING REMARKS

A numerical method was presented to calculate two-dimensional, time-dependent incompressible flows on non-orthogonal grids for high Reynolds numbers. Davis' high-resolution second-order-accurate scheme was extended to the IMM for resolving the non-linear vorticity equation. Constraints on the limiters, as functions of gradient ratios, have been used so that the resulting scheme is TVD. Roe's limiter and others such as minmod and Chakravarty–Osher limiters have been investigated. The Poisson equation was solved iteratively by an SOR method and the velocity field satisfied the continuity equation up to machine accuracy. The method is robust and easy to code. The test cases presented here were considered as standard problems to validate numerical methods in terms of both accuracy and efficiency. The examples shown are in good agreement with either numerical or

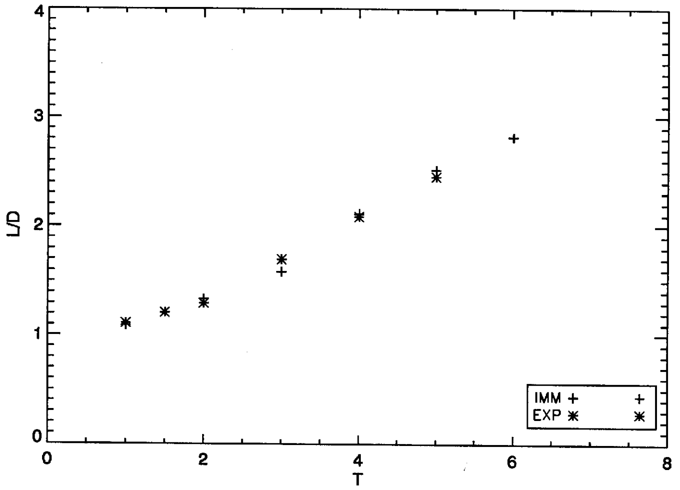

Figure 34. Comparison between experimental and numerical results for unsteady main wake length for $Re = 3000$

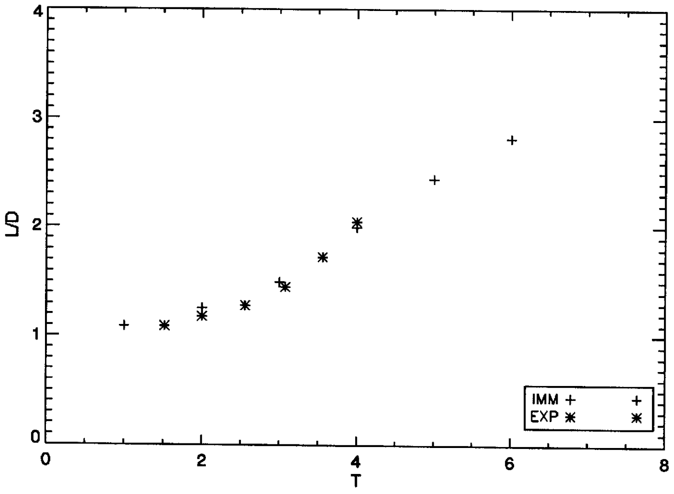

Figure 35. Comparison between experimental and numerical results for unsteady main-wake length for $Re = 9500$

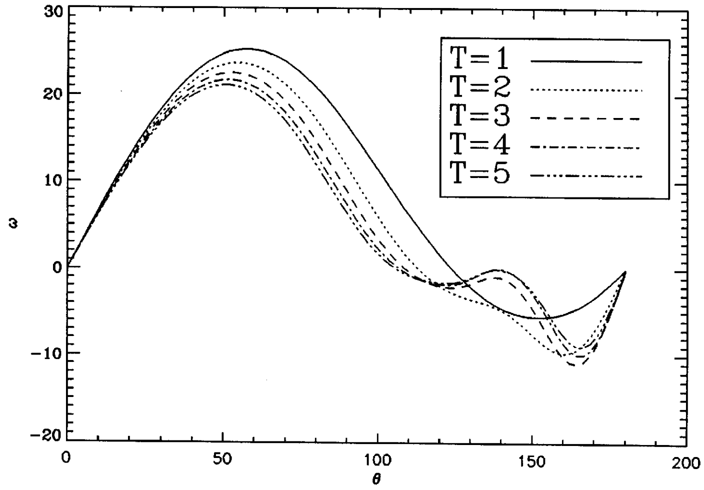

Figure 36. Evolution with time of vorticity repartition on surface of cylinder for $Re = 300$

experimental visualization results and can be considered as an illustration of the ability of the scheme to describe the details of complex steady or unsteady flows.

APPENDIX: EXTENSION OF DAVIS' APPROACH TO IMM

We consider the terms

$$-\Delta t\,\underbrace{(uf_x + vf_y)}_{\text{(a)}} + \underbrace{\frac{(\Delta tu)^2}{2}f_{xx} + \frac{(\Delta tv)^2}{2}f_{yy}}_{\text{(b)}} \tag{38}$$

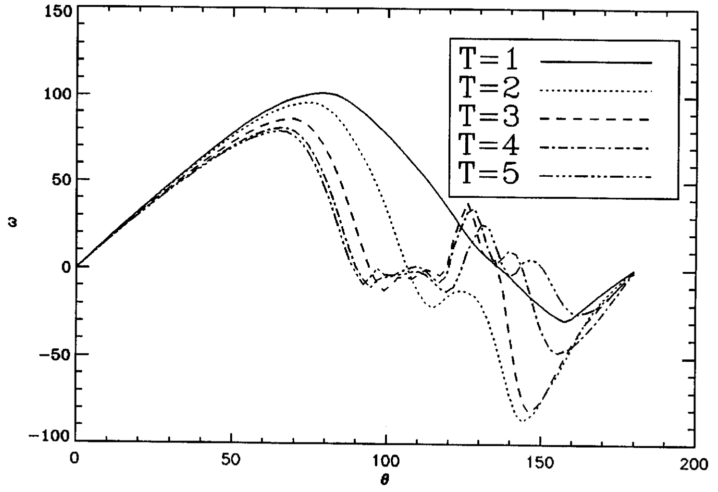

Figure 37. Evolution with time of vorticity repartition on surface of cylinder for $Re = 9500$

in the Lax–Wendroff scheme for a physical quantity $f = f(x, y, t)$. In the IMM the derivatives are written as

$$
\begin{aligned}
f_x = \frac{\partial f}{\partial x} &= coeff(1, 1, ij)(f_1 - f_{ij}) + coeff(2, 1, ij)(f_2 - f_{ij}) \\
&\quad + coeff(3, 1, ij)(f_3 - f_{ij}) + coeff(4, 1, ij)(f_4 - f_{ij}), \\
f_y = \frac{\partial f}{\partial y} &= coeff(1, 2, ij)(f_1 - f_{ij}) + coeff(2, 3, ij)(f_2 - f_{ij}) \\
&\quad + coeff(3, 1, ij)(f_3 - f_{ij}) + coeff(4, 2, ij)(f_4 - f_{ij}), \\
f_{xx} = \frac{\partial^2 f}{\partial x^2} &= coeff(1, 3, ij)(f_1 - f_{ij}) + coeff(2, 3, ij)(f_2 - f_{ij}) \\
&\quad + coeff(3, 3, ij)(f_3 - f_{ij}) + coeff(4, 3, ij)(f_4 - f_{ij}), \\
f_{yy} = \frac{\partial^2 f}{\partial y^2} &= coeff(1, 4, ij)(f_1 - f_{ij}) + coeff(2, 4, ij)(f_2 - f_{ij}) \\
&\quad + coeff(3, 4, ij)(f_3 - f_{ij}) + coeff(4, 4, ij)(f_4 - f_{ij}).
\end{aligned}
\qquad (39)
$$

To simplify the notation, we put

$$
\begin{array}{llll}
coeff(1, 1, ij) = C_{1x}, & coeff(2, 1, ij) = C_{2x}, & coeff(3, 1, ij) = C_{3x}, & coeff(4, 1, ij) = C_{4x}, \\
coeff(1, 2, ij) = C_{1y}, & coeff(2, 2, ij) = C_{2y}, & coeff(3, 2, ij) = C_{3y}, & coeff(4, 2, ij) = C_{4y}, \\
coeff(1, 3, ij) = C_{1xx}, & coeff(2, 3, ij) = C_{2xx}, & coeff(3, 3, ij) = C_{3xx}, & coeff(4, 3, ij) = C_{4xx}, \\
coeff(1, 4, ij) = C_{1yy}, & coeff(2, 4, ij) = C_{2yy}, & coeff(3, 4, ij) = C_{3yy}, & coeff(4, 4, ij) = C_{4yy},
\end{array}
$$

$\Delta f_{i+1/2} = f_3 - f_{ij}$, $\Delta f_{i-1/2} = f_{ij} - f_2$, $\Delta f_{j+1/2} = f_4 - f_{ij}$ and $\Delta f_{j-1/2} = f_{ij} - f_1$. Then the terms (a) in equations (38) takes the form

$$\begin{aligned} uf_x + vf_y &= (uC_{1x} + vC_{1y})(f_1 - f_{ij}) + (uC_{2x} + vC_{2y})(f_2 - f_{ij}) \\ &\quad + (uC_{3x} + vC_{3y}(f_3 - f_{ij}) + (uC_{4x} + vC_{4y})(f_4 - f_{ij}) \\ &= \underbrace{-(uC_{2x} + vC_{2y})\Delta f_{i-1/2} + (uC_{3x} + vC_{3y})\Delta f_{i+1/2}}_{\text{term in } x\text{: (c)}} \\ &\quad \underbrace{-(uC_{1x} + vC_{1y})\Delta f_{j-1/2} + (uC_{4x} + vC_{4y})\Delta f_{j+1/2}}_{\text{term in } y\text{: (d)}}. \end{aligned} \tag{40}$$

The coefficients are defined by

$$\begin{aligned} &C_{1x} = -\eta_x/2, &&C_{2x} = -\xi_x/2, &&C_{3x} = \xi_x/2, &&C_{4x} = \eta_x/2, \\ &C_{1y} = -\eta_y/2, &&C_{2y} = -\xi_y/2, &&C_{3y} = \xi_y/2, &&C_{4y} = \eta_y/2. \end{aligned}$$

Therefore

$$\begin{aligned} &-(uC_{2x} + vC_{2y}) = \tfrac{1}{2}(u\xi_x + v\xi_y) = \tfrac{1}{2}u', &&-(uC_{1x} + vC_{1y} = \tfrac{1}{2}(u\eta_x + v\eta_y) = \tfrac{1}{2}v', \\ &(uC_{3x} + vC_{3y}) = \tfrac{1}{2}(u\xi_x + v\xi_y) = \tfrac{1}{2}u', &&(uC_{4x} + vC_{4y}) = \tfrac{1}{2}(u\eta_x + v\eta_y) = \tfrac{1}{2}v', \\ &u' = u\xi_x + v\xi_y, \qquad v' = u\eta_x + v\eta_y, &&u' = 2(uC_{3x} + vC_{3y}), \qquad v' = 2(uC_{4x} + vC_{4y}). \end{aligned}$$

To extend the TVD concept to the Lax–Wendroff (L–W) centred scheme, the advective term is decantered in the following way. If $u' > 0$, the term (c) according to x is written as

$$\begin{aligned} &-(uC_{2x} + vC_{2y})\Delta f_{i-1/2} + (uC_{3x} + vC_{3y})\Delta f_{i+1/2} + (uC_{2x} + vC_{2y})\Delta f_{i-1/2} - (uC_{2x} + vC_{2y})\Delta f_{i-1/2} \\ &\quad = -2(uC_{2x} + vC_{2y})\Delta f_{i-1/2} + (uC_{3x} + vC_{3y})\Delta f_{i+1/2} + (uC_{2x} + vC_{2y})\Delta f_{i-1/2}. \end{aligned}$$

If $u' < 0$, the term according to x is written as

$$\begin{aligned} &-(uC_{2x} + vC_{2y})\Delta f_{i-1/2} + (uC_{3x} + vC_{3y})\Delta f_{i+1/2} + (uC_{3x} + vC_{3y})\Delta f_{i+1/2} - (uC_{3x} + vC_{3y})\Delta f_{i+1/2} \\ &\quad = -(uC_{2x} + vC_{2y})\Delta f_{i-1/2} + 2(uC_{3x} + vC_{3y})\Delta f_{i+1/2} - (uC_{3x} + vC_{3y})\Delta f_{i+1/2}. \end{aligned}$$

If $v' > 0$, the term (d) according to y is written as

$$\begin{aligned} &-(uC_{1x} + vC_{1y})\Delta f_{j-1/2} + (uC_{4x} + vC_{4y})\Delta f_{j+1/2} + (uC_{1x} + vC_{1y})\Delta f_{i-1/2} - (uC_{1x} + vC_{1y})\Delta f_{j-1/2} \\ &\quad = -2(uC_{1x} + vC_{1y})\Delta f_{j-1/2} + (uC_{4x} + vC_{4y})\Delta f_{j+1/2} + (uC_{1x} + vC_{1y})\Delta f_{j-1/2}. \end{aligned}$$

If $v' < 0$ the term according to y is written as

$$\begin{aligned} &-(uC_{1x} + vC_{1y})\Delta f_{j-1/2} + (uC_{4x} + vC_{4y})\Delta f_{j+1/2} + (uC_{4x} + vC_{4y})\Delta f_{j+1/2} - (uC_{4x} + vC_{4y})\Delta f_{j+1/2} \\ &\quad = -(uC_{1x} + vC_{1y})\Delta f_{j-1/2} + 2(uC_{4x} + vC_{4y})\Delta f_{j+1/2} - (uC_{4x} + vC_{4y})\Delta f_{j+1/2}. \end{aligned}$$

The term (b) of second order in equation (38) is written as

$$\begin{aligned} &-\frac{\Delta t^2}{2}(u^2C_{1xx} + v^2C_{1yy})\Delta f_{j-1/2} - \frac{\Delta t^2}{2}(u^2C_{2xx} + v^2C_{2yy})\Delta f_{i-1/2} \\ &\quad + \frac{\Delta t^2}{2}(u^2C_{3xx} + v^2C_{3yy})\Delta f_{i+1/2} + \frac{\Delta t^2}{2}(u^2C_{4xx} + v^2C_{4yy})\Delta f_{j+1/2}. \end{aligned} \tag{41}$$

The L–W scheme is written as

$$f_{ij}^{n+1} = f_{ij}^{n} - \Delta t(uf_x + vf_y) + \frac{(u\Delta t)^2}{2} f_{xx} + \frac{(v\Delta t)^2}{2} f_{yy}. \tag{42}$$

When the contravariant velocities u' and v' are positive, the scheme takes the form

$$\begin{aligned} f_{ij}^{n+1} = f_{ij}^{n} &- \Delta t[-2(uC_{2x} + vC_{2y})\Delta f_{i-1/2} + (uC_{3x} + vC_{3y})\Delta f_{i+1/2} + (uC_{2x} + vC_{2y})\Delta f_{i-1/2}] \\ &+ \frac{\Delta t^2}{2}(u^2 C_{3xx} + v^2 C_{3yy})\Delta f_{i+1/2} - \frac{\Delta t^2}{2}(u^2 C_{2xx} + v^2 C_{2yy})\Delta f_{i-1,2} - \Delta t[-2(uC_{1x} + vC_{1y})\Delta f_{j-1/2} \\ &+ (uC_{4x} + vC_{4y})\Delta f_{j+1/2} + (uC_{1x} + vC_{1y}) f_{j-1/2}] + \frac{\Delta t^2}{2}(u^2 C_{4xx} + v^2 C_{4yy})\Delta f_{j+1/2} \\ &- \frac{\Delta t^2}{2}(u^2 C_{1xx} + v^2 C_{1yy})\Delta f_{j-1/2}. \end{aligned} \tag{43}$$

Introducing the flux limiters $\Phi_{i+1/2}$, $\Phi_{i+1/2}$, $\Phi_{j+1/2}$ and $\Phi_{j-1/2}$ as in Davis' approach, we obtain

$$\begin{aligned} f_{ij}^{n+1} = f_{ij}^{n} &- \Delta t[-2(uC_{2x} + vC_{2y})\Delta f_{i-1/2}] - \left(\Delta t(uC_{3x} + vC_{3y}) - \frac{\Delta t^2}{2}(u^2 C_{3xx} + v^2 C_{3yy})\right)\Phi_{i+1/2}\Delta f_{i+1/2} \\ &- \left(\Delta t(uC_{2x} + vC_{2y}) + \frac{\Delta t^2}{2}(u^2 C_{2xx} + v^2 C_{2yy})\right)\Phi_{i-1/2}\Delta f_{i-1/2} - \Delta t[-2(uC_{1x} + vC_{1y})\Delta f_{j-1/2}] \\ &- \left(\Delta t(uC_{4x} + vC_{4y}) - \frac{\Delta t^2}{2}(u^2 C_{4xx} + v^2 C_{4yy})\right)\Phi_{j+1/2}\Delta f_{j+1/2} \\ &- \left(\Delta t(uC_{4x} + vC_{4y}) + \frac{\Delta t^2}{2}(u^2 C_{1xx} + v^2 C_{1yy})\right)\Phi_{j-1/2}\Delta f_{j-1/2}. \end{aligned} \tag{44}$$

Rewriting the global scheme in the form

$$\text{L–W} + (K_{i+1/2}^{+}\Delta f_{i+1/2} - K_{i-1/2}^{+}\Delta f_{i-1/2}) + (K_{j+1/2}^{+}\Delta f_{j+1/2} - K_{j-1/2}^{+}\Delta f_{j-1/2}) \tag{45}$$

gives the following equalities according to equations (44) and (45):

$$\begin{aligned} \left(\Delta t(uC_{3x} + vC_{3y}) - \frac{\Delta t^2}{2}(u^2 C_{3xx} + v^2 C_{3yy})\right)\Phi_{i+1/2} &= \left(\Delta t(uC_{3x} + vC_{3y}) - \frac{\Delta t^2}{2}(u^2 C_{3xx} + v^2 C_{3yy})\right) \\ &\quad - K_{i+1/2}^{+}, \\ \left(\Delta t(uC_{2x} + vC_{2y}) + \frac{\Delta t^2}{2}(u^2 C_{2xx} + v^2 C_{2yy})\right)\Phi_{i-1/2} &= \left(\Delta t(uC_{2x} + vC_{2y}) + \frac{\Delta t^2}{2}(u^2 C_{2xx} + v^2 C_{2yy})\right) \\ &\quad + K_{i-1/2}^{+}. \end{aligned}$$

Then we obtain by identification the expression of the dissipation terms as

$$\begin{aligned} K_{i+1/2}^{+} &= \left(\Delta t(uC_{3x} + vC_{3y}) - \frac{\Delta t^2}{2}(u^2 C_{3xx} + v^2 C_{3yy})\right)(1 - \Phi_{i+1/2}), \\ K_{i=1/2}^{+} &= \left(\Delta t(uC_{2x} + vC_{2y}) + \frac{\Delta t^2}{2}(u^2 C_{2xx} + v^2 C_{2yy})\right)(\Phi_{i-1/2} - 1). \end{aligned} \tag{46}$$

Likewise, according to y,

$$\begin{aligned} K^{+}_{j+1/2} &= \left(\Delta t(uC_{4x} + vC_{4y}) - \frac{\Delta t^2}{2}(u^2 C_{4xx} + v^2 C_{4yy})\right)(1 - \Phi_{j+1/2}),\\ K^{+}_{j+1/2} &= \left(\Delta t(uC_{1x} + vC_{1y}) + \frac{\Delta t^2}{2}(u^2 C_{1xx} + v^2 C_{1yy})\right)(\Phi_{j-1/2} - 1). \end{aligned} \tag{47}$$

With $u' < 0$ the expression of the dissipation terms takes the form

$$\begin{aligned} K^{-}_{i+1/2} &= \left(\Delta t(uC_{3x} + vC_{3y}) + \frac{\Delta t^2}{2}(u^2 C_{3xx} + v^2 C_{3yy})\right)(\Phi_{i+1/2} - 1),\\ K^{-}_{i-1/2} &= \left(\Delta t(uC_{2x} + vC_{2y}) - \frac{\Delta t^2}{2}(u^2 C_{2xx} + v^2 C_{2yy})\right)(1 - \Phi_{i-1/2}). \end{aligned} \tag{48}$$

With $v' < 0$ the expression of the dissipation terms takes the form:

$$\begin{aligned} K^{-}_{j+1/2} &= \left(\Delta t(uC_{4x} + vC_{4y}) + \frac{\Delta t^2}{2}(u^2 C_{4xx} + v^2 C_{4yy})\right)(\Phi_{i+1/2} - 1),\\ K^{-}_{j-1/2} &= \left(\Delta t(uC_{1x} + vC_{1y}) - \frac{\Delta t^2}{2}(u^2 C_{1xx} + v^2 C_{1yy})\right)(1 - \Phi_{i-1/2}). \end{aligned} \tag{49}$$

REFERENCES

1. S. Koshizuka, Y. Oka, S. Kondo and Y. Togo, ‘Interpolating matrix method: a finite difference method for arbitrary arrangement of mesh points’, *J. Comput. Phys.*, **75**, 444–468 (1988).
2. K. D. Nguyen and H. En-Nefkhaoui, ‘Numerical simulation of viscous flows in complex geometries by the interpolation matrix method’, *Proc. 5th Int. Symp. on Computational Fluid Dynamics*, Sendai, Japan, 1993, Vol. 2, pp. 351–356.
3. L. Hanich, M. Louaked and K. D. Nguyen, ‘Simulation numérique de l’écoulement instationnaire autour d’un cylindre par une méthode TVD–matrices d’interpolation’, *12me Congr. Fr. de Mécanique*, Strasbourg, September 1995, Vol. 2, pp. 153–156.
4. L. Hanich, ‘Résolution des équations de la mécanique des fluides par des méthodes TVD en coordonnées généralisées’, *Ph.D. Thesis*, University of Caen, 1996.
5. M. Louaked, L. Hanich and K. D. Nguyen, ‘An improved TVD scheme to resolve the Navier–Stokes equations in stream–vorticity formulation by the interpolating matrix method’, in W. H. Hui, Y. K. Kwok and J. R. Chasnov (eds), *Proc. First Asian Computational Fluid Dynamics Conf.*, Hong Kong, 1995, Vol. 2, pp. 421–426.
6. M. Louaked, L. Hanich and K. D. Nguyen, ‘High resolution of the 2D Navier–Stokes equations by the interpolating matrix method’, in K. W. Morton and M. J. Baines (eds), *Numerical Methods for Fluid Dynamics V*, Oxford Universitys Press, Oxford, 1996, pp. 457–464.
7. A. Harten, ‘On a class of high resolution total variation stable finite difference schemes’, *SIAM J. Numer. Anal.*, **21**, 1–23 (1984).
8. F. Davis, ‘TVD finite difference schemes and artificial viscosity’, *ICASE Rep. 84–20*, 1984.
9. P. Sweby, ‘High-resolution schemes using flux limiters for hyperbolic conservation laws’, *SIAM J. Numer. Anal.*, **21**, 995–1011 (1984).
10. R. Peyret and T. D. Taylor, *Computational Methods for Fluid Flow*, Springer, Berlin, 1983.
11. R. Bouard and M. Coutanceau, ‘The early stage of development of the wake behind an impulsively started cylinder for 40 < *Re* < 104’, *J. Fluid Mech.*, **101**, 583 (1980).
12. Ta Phuoc Loc, ‘Numerical analysis of unsteady secondary vortices generated by an impulsively started circular cylinder’, *J. Fluid Mech.*, **100**, 111 (1980).
13. Ta Phuoc Loc and R. Bouard, ‘Numerical solution of the early stage of the unsteady viscous flow around a circular cylinder with experimental visualization and measurements’, *J. Fluid Mech.*, **160**, 93–117 (1985).
14. I. Demirdzic, Ž. Lilek and M. Perić, ‘Fluid flow and heat transfer test problems for non-orthogonal grids: bench-mark solutions’, *Int. j. numer. methods fluids*, **15**, 329–354 (1992).
15. C. W. Oosterlee, P. Wesseling, A. Segal and E. Brakkee, ‘Benchmark solutions for the incompressible Navier–Stokes equations in general co-ordinates on staggered grids’, *Int. j. number. methods fluids*, **17**, 301–321 (1993).
16. Ch.-H. Bruneau and P. Fabrie, ‘Effective downstream boundary conditions for incompressible Navier–Stokes equations’, *Int. j. numer. methods fluids*, **19**, 693–705 (1994).

17. O. Daube and Ta Phuoc Loc, 'Étude numérique d'écoulement instationnaires de fluide visqueux incompressible autour de corps profilés par une méthode dombinée d'ordre $O(h^2)$ et $O(h^4)$, *J. Méc.*, **17**, (1978).
18. M.-H. Chou and W. Huang, 'Numerical study of high-Reynolds-number flow past a bluff object', *Int. j. numer. methods fluids*, **23**, 711–732 (1996).
19. A. Borthwick, 'Comparision between two finite-difference schemes for computing flow around a cylinder', *Int. j. numer. methods fluids*, **6**, 275–290 (1986).
20. O. Daube, 'Resolution of 2D Navier–Stokes equations in velocity–vorticity form by means of an influence matrix technique', *J. Comput. Phys.*, **103**, 402–414 (1992).
21. A. Harten, B. Engquist, S. Osher and S. Chakravarty, 'Uniformly high order accurate essentially nonoscillatory schemes, II', *J. Comput. Phys.*, **71**, 231 (1987).
22. A. Jameson, 'A nonoscillatory shock capturing scheme using flux limited dissipation', *Lect. Appl. Math.*, **22**, (1985).
23. P. D. Koumoutsakos, 'Direct numerical simulations of unsteady separated flows using vortex methods', *Ph.D. Thesis*, California Institute of Technology, Pasadena, CA, 1993.
24. F. Pépin, 'Simulation of the flow past an impulsively started cylinder using a discrete vortex method', *Ph.D. Thesis*, California Institute of Technology, Pasadena, CA, 1990.
25. P. L. Roe, 'Generalized formulation of TVD Lax–Wendroff schemes', *ICASE Rep. 84–53*, 1984.
26. D. Sidilkover and P. L. Roe, 'Unification of some advection schemes in two dimensions', *ICASE Rep. 10-95*, 1995.
27. H. Yee 'Construction of explicit and implicit symmetric TVD schemes and their applications', *J. Comput. Phys.*, **68**, 151–179 (1987).